Simulation-Based Joint Estimation of Body Deformation and Elasticity Parameters for Medical Image Analysis

Huai-Ping Lee*, Mark Foskey, Marc Niethammer, Pavel Krajcevski, and Ming C. Lin, *Fellow, IEEE*

***Abstract*—Estimation of tissue stiffness is an important means of noninvasive cancer detection. Existing elasticity reconstruction methods usually depend on a dense displacement field (inferred from ultrasound or MR images) and known external forces. Many imaging modalities, however, cannot provide details within an organ and therefore cannot provide such a displacement field. Furthermore, force exertion and measurement can be difficult for some internal organs, making boundary forces another missing parameter. We propose a general method for estimating elasticity and boundary forces automatically using an iterative optimization framework, given the desired (target) output surface. During the optimization, the input model is deformed by the simulator, and an objective function based on the distance between the deformed surface and the target surface is minimized numerically. The optimization framework does not depend on a particular simulation method and is therefore suitable for different physical models. We show a positive correlation between clinical prostate cancer stage (a clinical measure of severity) and the recovered elasticity of the organ. Since the surface correspondence is established, our method also provides a non-rigid image registration, where the quality of the deformation fields is guaranteed, as they are computed using a physics-based simulation.**

***Index Terms*—Elasticity reconstruction, Physically-based simulation, Non-rigid image registration.**

I. Introduction

MATERIAL property estimation has been an important topic in noninvasive cancer diagnosis, since cancerous tissues tend to be stiffer than normal tissues. Traditional physical examination methods, such as palpation, are limited to detecting lesions close to the skin, and reproducible measurements are hard to achieve. With the advance of medical imaging technologies, it becomes possible to quantitatively study the material properties using noninvasive procedures.

Computer vision methods in combination with force or pressure sensing devices have been proposed to find material properties of tissues [1], [2]. These methods require a controlled environment in order to capture the video and force (pressure), and therefore the experiments are usually done *ex vivo*. Kauer et al. [1] combined the video and pressure capturing components into a single device to simplify the measurement process, so that it can be performed *in vivo* during a surgical intervention. However, the device still needs to be in direct contact with the tissue, and only a small portion of the tissue can be measured due to the size of the device.

Elasticity reconstruction, or elastography, is a noninvasive method for acquiring strain or stiffness images using known external forces and a known displacement field [3], [4]. The reconstruction is usually formulated as an inverse problem of a physically-based simulation of elastic bodies, and a popular choice of the simulator is based on a linear elasticity model solved with the finite element method (FEM) [5], where the domain of the image is subdivided into tetrahedrons or hexahedrons called *elements*, with vertices known as *nodes*. Boundary conditions (displacement vectors or forces) on some of the nodes must be given to drive the simulation. Under this framework, nodal displacement vectors need to be computed based on a pair of images, and the force exertion mechanism needs to be controlled so that external forces can be measured. Otherwise, without measured forces, only relative elasticity values can be recovered. Ultrasound elastography [6], for example, compares two ultrasound images, one taken at the rest pose, and the other taken when a known force is applied. The displacement vector for each pixel can be estimated using cross-correlation analysis [3], [7] or dynamic programming [8] to maximize the similarity of echo amplitude and displacement continuity. Alternatively, in dynamic elastography (for example, magnetic resonance elastography (MRE) and vibro-elastography), an MRI or ultrasound machine in tune with an applied mechanical vibration (shear wave) or focused ultrasound beams is used to find the displacement field [4], [9], [10]. With known external forces and displacement field, the elasticity can be computed by solving a least-squares problem [11], [12], [13], if the algebraic equations resulting from the physical model is linear. A real-time performance has been reported using this *direct* method with a simplified 2D domain that assumes homogeneous material within a region [13]. Another type of method uses iterative optimization to minimize the error in the displacement field generated by the simulator [14], [15], [16]. Although slower than directly solving the inverse problem, this type of method does not assume linearity of the underlying physical model. A different kind of elastography [17], [18], [19] maximizes image similarity without requiring the displacement field or boundary conditions to be known, but the method relies on salient features within the object (such as the breast), which may

*Huai-Ping Lee is with Department of Computer Science, University of North Carolina, Chapel Hill, NC 27599 USA (email: lhp@cs.unc.edu).

Mark Foskey, Marc Niethammer, Pavel Krajcevski, and Ming C. Lin are with Department of Computer Science, University of North Carolina, Chapel Hill, NC 27599 USA; Mark Foskey is also with Morphormics, Inc., Durham, NC 27707 USA; Marc Niethammer is also with the Biomedical Research Imaging Center (BRIC), University of North Carolina, Chapel Hill, NC 27599 USA.

not be present in CT images of organs such as the prostate. A phantom study applied the method to the prostate [18], but the model and boundary conditions are greatly simplified, and their method has not been applied to real patient data. A Bayesian framework has also been proposed to solve the elastography problem without requiring known boundary conditions [20]. That method, however, depends on assumptions about probability distribution functions and extensive sampling in a very high dimensional parameter space (elasticity and boundary conditions), which significantly limits the number of boundary nodes. While these methods are instrumental in their respective fields of interest, they are less well suited for a more general, multi-organ case where the image intensity may be almost constant within an organ, such as the prostate, and the lack of image details within the object makes it impossible to rely on pixel-wise correspondence. Moreover, the force exertion or vibration actuation mechanism can become complicated when the target tissues are deep inside the body. For example, for an elastography of the prostate, an actuator or a pressure sensor is sometimes inserted into the urethra or the rectum [21], [9], [22].

Elasticity parameters are also essential in cardiac function estimation, where sequential data assimilation [23], [24] has been applied to estimate simulation parameters and displacements simultaneously for dynamic mechanical systems. The parameters and observations of displacements (*states*) at each time step are modeled with a probability distribution, and a filtering procedure is applied over some time to estimate the states. Due to the computational complexity of the method, the number of estimated parameters has been very limited in work on cardiac function estimation [23]. On the other hand, our parameter space includes external forces as well as the Young's modulus, and the displacement field cannot be acquired directly from some common imaging modality like CT.

We propose an entirely passive analysis of a pair of images that only uses information about the boundaries of corresponding internal objects. We assume the images have already been segmented, that is, the organ boundaries have been found. Since we do not assume a good correspondence for pixels inside an object, the resolution of the resulting elastogram is limited to the object boundaries. Namely, we assume that the elasticity is fixed within each object whose boundary can be identified. Natural movements inside the body provide the deformation of the organs, and we do not need an additional force exertion or vibration actuating mechanism. We minimize the distance between the deformed reference surface and the target surface and optimize for the elasticities and boundary forces. Currently, as a simplification, we consider only Young's modulus (which measures the stiffness or elasticity of the material). It is the simplest parameter to work with, and it is also important in noninvasive cancer detection techniques. The general optimization framework extends naturally to the inclusion of other parameters such as Poisson's ratio (which measures compressibility of the material), and in fact is suitable for a variety of physical models. In our experiments, the images are obtained from a prostate radiotherapy, where there is one reference (planning) CT image and multiple target (daily) images for each patient, and the Young's moduli of the prostate recovered from the pairs of images are averaged. Our initial investigation involving 10 patient data sets shows that the recovered elasticity values positively correlate with the clinical tumor stages, which demonstrates its potential as a means of cancer stage assessment complementary to existing elastography methods. Furthermore, compared broadly to other work on simulation parameter estimation, our method does not require the inclusion of forces as part of the input and can therefore avoid the process of measuring the external forces (at the cost of only providing relative force information in our results).

Our method also produces an image registration [25], [26] (pixel-wise correspondence between images) since the distance between the pair of surfaces (segmentations) is minimized. The FEM has been applied to image registration, given that the images are segmented [27], [28], [29], [30], [31], [32], [33]. Material properties, however, are not trivial to find from the images, and most authors use *ex vivo* experimental results to set up the materials. Moreover, due to the patient-to-patient differences, these material properties sometimes need hand adjustments. Alterovitz et al. [34] incorporated an optimization of Young's modulus and Poisson's ratio into an FEM-based registration, but the method has only been implemented for coarse 2D meshes. As a non-rigid image registration method, ours improves over previous simulation-based methods by providing an automatic means of finding the parameters that are missing in the images. Our current implementation uses both standard linear and nonlinear material models, but the optimization framework should be applicable to tissues with more advanced and complex physical models.

We explain the elastic model and the optimization scheme in Section II, followed in Section III by experimental results using two synthetic scenes and 10 sets of real CT images to demonstrate the feasibility of our method. We conclude with a summary and discussion of future work.

II. Method

The idea of the algorithm is to optimize a function based on the separation between corresponding organ boundaries. In each iteration, the objective function is computed by first simulating and deforming the surface using the current set of parameters, and then computing surface distances. We consider only the elasticity value (Young's modulus), with Poisson's ratios being chosen according to previous work on simulation-based medical image registration [31].

The inputs to the correspondence problem are two segmented images: a fixed image with segmentation $\mathbf{S}_f$ and a moving image with segmentation $\mathbf{S}_m$. The bones are already aligned using a rigid registration method described in [35]. Each segmentation is represented as a set of closed triangulated surfaces, one for each segmented object. We construct a tetrahedralization of the moving volume such that each face of $\mathbf{S}_m$ is a face in the tetrahedralization, so that $\mathbf{S}_m$ is characterized entirely by its set of nodes. Our optimization framework is built on a physically-based simulator that generates deformation fields with n unknown

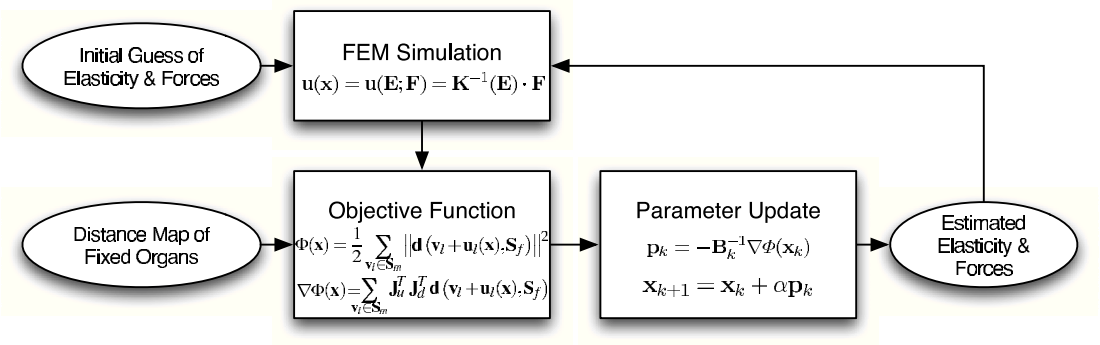

Figure 1: Flow chart of the optimization loop; the deformation field generated by the simulator is used in the objective function to update the parameters, which are fed back into the simulator, and so on.

parameters $\mathbf{x} = [x_1, \cdots, x_n]^T$, and a numerical optimizer to minimize an objective function $\Phi(\mathbf{x}) : \mathbb{R}^n \rightarrow \mathbb{R}$ defined by the deformation and surface matching metrics. During the optimization process, the physical model is refined in terms of more accurate parameters and converges to a model describing the deformation needed for the particular surface matching problem. Here we use the linear FEM to illustrate the optimization scheme, although the framework can also be incorporated with a nonlinear FEM. A flow chart of our algorithm is shown in Fig. 1 and will be explained in detail in this section.

A. Linear Elasticity Model and Finite Element Modeling

In the optimization loop, the displacement field $\mathbf{u} = [u, v, w]^T$ is always generated by a physically-based simulation, where the FEM is used to solve the constitutive equations of the linear elasticity model. Assuming isotropic linear elasticity, we can write $\sigma = \mathbf{D}\varepsilon$, where σ is the stress vector induced by the *surface forces*, ε is the strain vector defined by the spatial derivatives of the displacement $\mathbf{u}$, and $\mathbf{D}$ is a matrix defined by the material properties (assuming an isotropic material, the properties are Young's modulus E and Poisson's ratio ν). To solve the equations numerically, we approximate the derivatives of the deformation with the FEM, where the domain is subdivided into a finite set of elements, and each element consists of several nodes. Fig. 4a shows the finite element model used in one of our experiments, where four-node tetrahedral elements are used. The deformation field $\mathbf{u}^{el}$ for any point $\mathbf{p}$ within an element is approximated with a piecewise linear function $\hat{\mathbf{u}}^{el}(\mathbf{p}) = \sum_{j=1}^{4} \mathbf{u}_j^{el} N_j^{el}(\mathbf{p})$, where $\mathbf{u}_j^{el}$ is the deformation of the j-th node of the element, and $N_j^{el}(\mathbf{p})$ is the linear shape function that has value one at node j and is zero at all other nodes and outside of the element. After combining the approximated piecewise linear equation for each element, the resulting linear system is

$$\mathbf{K}\mathbf{u} = \mathbf{F}, \tag{1}$$

where $\mathbf{K}$ is called the stiffness matrix, which depends on the material properties (Young's modulus and Poisson's ratio) and the geometry of the elements; $\mathbf{F}$ is a vector of external forces. For a 3D domain with N_n nodes, $\mathbf{K}$ is a $3N_n \times 3N_n$ matrix. Notice that since both $\mathbf{K}$ and $\mathbf{F}$ are unknown, they can be scaled by the same factor without changing the output deformation field. Therefore, unless we know the exact values of the forces, only the relative values of the material properties can be recovered.

To make the nodes deform, some boundary conditions need to be enforced, either by assigning displacement values or by assigning forces to some nodes. If all the surface nodes, including boundaries between two materials, are assigned displacement values, then the simulation is essentially an interpolation of the displacement field from surface matching results. This means that the elasticity values only affect internal nodes, for which we do not know the target positions. Therefore the elasticity cannot be recovered. Instead, we only assign boundary conditions to a part of the surface nodes, and other surface nodes without boundary conditions will be affected by the relative elasticities. For example, in a simulation of the male pelvis area, the bladder and the rectum are usually the organs that drive the deformation of the prostate, while the pelvic bone is considered static. An intuitive choice is to apply boundary conditions on boundary nodes of the bladder, the rectum, and the pelvic bone, and set all other entries in the force vector to zero (no external forces), as proposed in [31].

B. Sensitivity Study

Since our method is based on the assumption that the deformed surface depends on both the elasticity and the external forces, we first conduct an experiment of forward simulations using different parameter values to see how sensitive the surface is to these parameters. The synthetic scene consists of two concentric spheres that form two regions, one inside the inner sphere, and the other between the two spheres, as shown in Fig. 2.

We fix the elasticity of the outer region and alter the elasticity of the inner sphere, as only the ratio of the two elasticity values matters. A force with a specified magnitude pointing towards the center of the spheres is applied on each node of the outer surface, and no external forces are applied on the inner surface. Several simulations using different elasticities of the inner region and force magnitudes were performed, and the plots of the sphere radius versus the elasticity value and versus force magnitude are shown in Fig. 3.

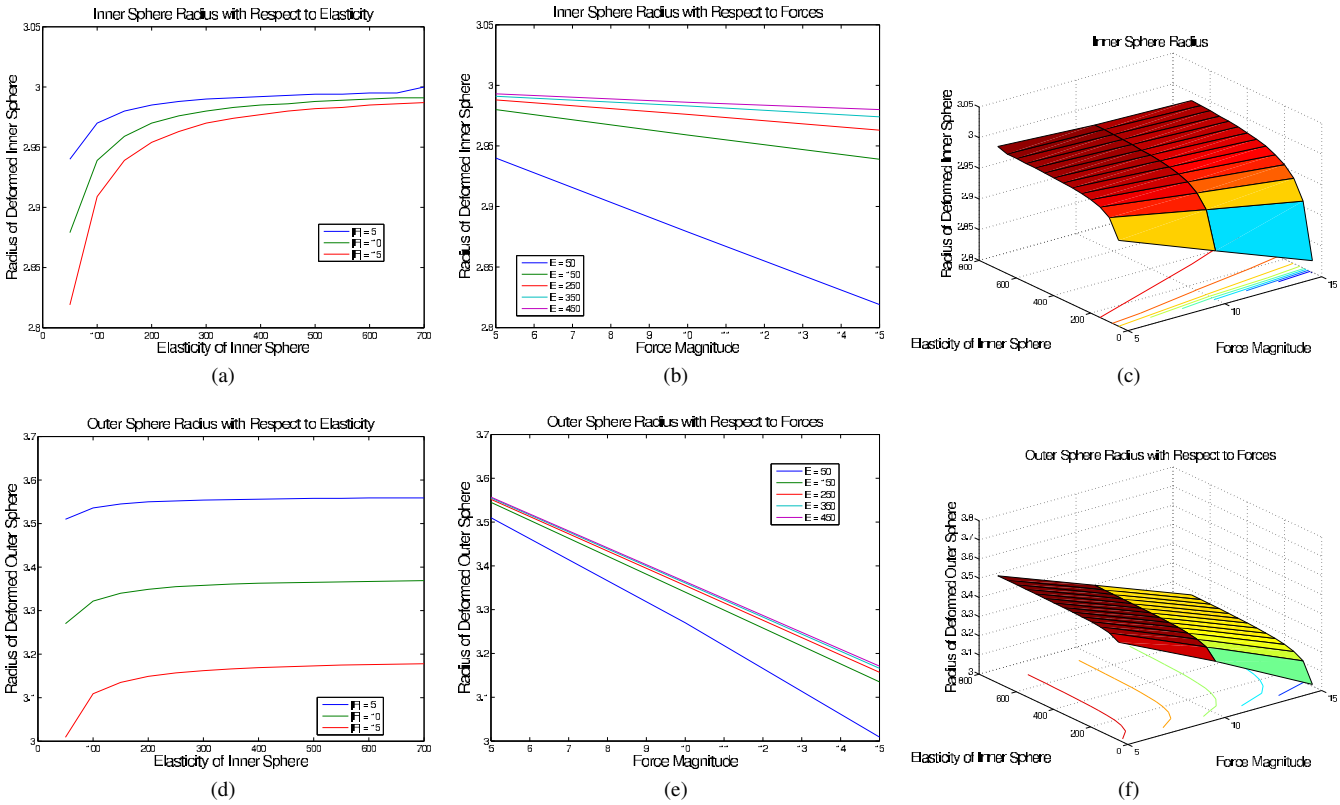

(a) (b) (c)

(d) (e) (f)

Figure 3: The plots of the radius of the inner sphere (in cm) after deformation: (a) inner radius versus elasticity value (in kPa) of the inner region; (b) inner radius versus magnitude of forces (in N) acting on the outer surface; (c) inner radius (z-coordinate) versus elasticity and force magnitude with isocontours of inner radius on xy-plane; (d) outer radius versus elasticity; (e) outer radius versus magnitude of forces; (f) outer radius (z-coordinate) versus elasticity and force magnitude with isocontours of outer radius on xy-plane. The radii before deformation are 3 cm and 3.75 cm for two spheres, respectively, and the elasticity for the outer region is 10 kPa. The Poisson's ratios are fixed to 0.40 and 0.35 for the two regions, respectively.

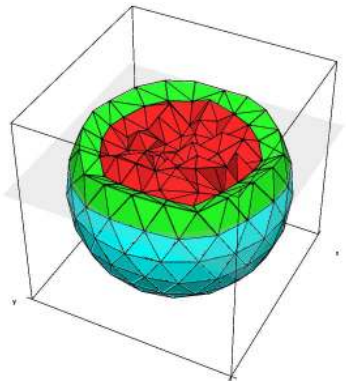

Figure 2: A sliced view of the synthetic scene, which consists of two concentric spheres; the inner (red) and outer (green) regions have different stiffness values (blue triangles represent outer surface, which is considered part of the green region).

Notice that in these plots, the slope is much higher when the elasticity is low for each curve, which indicates that the shapes of both spheres are much more sensitive to the elasticity when the elasticity value is lower. These results suggest that our ability to recover the parameters is limited by how stiff the object is. When an object has a very high stiffness, its shape becomes insensitive to the parameters. In this case, the shape can still be recovered, but the resulting parameters may not be accurate. Notice that the problem of solving for elasticity and for boundary forces is ill-posed with a single object. For example, drawing horizontal lines at some inner radius value in the plots in Fig. 3 would give multiple combinations of elasticity and external forces. However, when both the inner and outer surfaces are taken into account, the problem becomes well-posed: in the two-dimensional space formed by elasticity value and force magnitude, there is one curve that implies some radius of the inner sphere (an isocontour on the xy-plane in Fig. 3c) and another curve that results in some radius of the outer sphere (an isocontour on the xy-plane in Fig. 3f). The solution is at one of the intersections of the two curves, and we can eliminate unwanted solutions by limiting the range of elasticity and force magnitude according to experimental results on the specific materials.

C. Distance-Based Objective Function

The parameters needed in the simulator are $\mathbf{x} = [\mathbf{E}; \mathbf{F}]$, where $\mathbf{E}$ consists of the material properties (in our case, the Young's moduli), and $\mathbf{F}$ is the vector of external forces on

boundary nodes. The objective function to be minimized is defined as the difference between the segmentations in the moving and target images,

$$\Phi(\mathbf{x}) = \frac{1}{2} \sum_{\mathbf{v}_l \in \mathbf{S}_m} \left\| \mathbf{d}\left(\mathbf{v}_l + \mathbf{u}_l(\mathbf{x}), \mathbf{S}_f\right) \right\|^2 . \tag{2}$$

Here $\mathbf{u}(\mathbf{x})$ is the deformation field computed by the simulator with parameters $\mathbf{x}$, interpreted as a displacement vector for each surface node $\mathbf{v}_l$ in the tetrahedralization. The notation $\mathbf{d}(\mathbf{v}, \mathbf{S})$ denotes the shortest distance vector from the surface $\mathbf{S}$ to the node $\mathbf{v}$, and the sum is taken over all nodes of the moving surface.

The gradient of the objective function, which is needed in the iterative optimization, is given by the chain rule,

$$\begin{aligned} \nabla\Phi(\mathbf{x}) &= \sum_{\mathbf{v}_l \in \mathbf{S}_m} \left[\frac{\partial \mathbf{u}_l}{\partial \mathbf{x}}\right] \left[\frac{\partial \mathbf{d}\left(\mathbf{v}_l + \mathbf{u}_l, \mathbf{S}_f\right)}{\partial \mathbf{u}_l}\right] \mathbf{d}\left(\mathbf{v}_l + \mathbf{u}_l, \mathbf{S}_f\right) \\ &= \sum_{\mathbf{v}_l \in \mathbf{S}_m} \mathbf{J}_u^T \, \mathbf{J}_d^T \, \mathbf{d}\left(\mathbf{v}_l + \mathbf{u}_l, \mathbf{S}_f\right), \end{aligned} \tag{3}$$

where $\mathbf{J}_u = \left[\frac{\partial u_i}{\partial x_j}\right]$ is the Jacobian matrix of $\mathbf{u}(\mathbf{x})$ with respect to the parameters, and $\mathbf{J}_d = \left[\frac{\partial d_i}{\partial u_j}\right]$ is the Jacobian matrix of $\mathbf{d}$ with respect to the deformation vector. Here we use the bracket $[\cdot]$ to represent a matrix and the curly braces $\{\cdot\}$ to denote a vector. Each column of $\mathbf{J}_d$, namely $\left\{\frac{\partial \mathbf{d}(\mathbf{v}_l+\mathbf{u}_l, \mathbf{S}_f)}{\partial u_j}\right\}$, is the derivative of $\mathbf{d}\left(\mathbf{v}_l + \mathbf{u}_l, \mathbf{S}_f\right)$ with respect to the j-th spatial coordinate ($j = 1, 2, 3$). The derivatives of $\mathbf{u}$ with respect to the material properties are computed by differentiating both sides of (1),

$$\left[\frac{\partial \mathbf{K}}{\partial E_j}\right] \mathbf{u} + \mathbf{K} \left\{\frac{\partial \mathbf{u}}{\partial E_j}\right\} = 0, \tag{4}$$

Therefore we have $\left\{\frac{\partial \mathbf{u}}{\partial E_j}\right\} = -\mathbf{K}^{-1} \left[\frac{\partial \mathbf{K}}{\partial E_j}\right] \mathbf{u}$. The Jacobian matrix can then be computed by solving for each column of $\mathbf{J}_u$. The derivatives with respect to the boundary forces are computed in the same manner; by taking derivatives of both sides of (1), we have $\left[\frac{\partial \mathbf{K}}{\partial F_j}\right] \mathbf{u} + \mathbf{K} \left\{\frac{\partial \mathbf{u}}{\partial F_j}\right\} = \mathbf{e}_j$, where $\mathbf{e}_j$ is the j-th coordinate vector. On the right hand side, only the j-th entry is nonzero since $\frac{dF_i}{dF_j} = 0$ when $i \neq j$. And since $\mathbf{K}$ is independent of F_j, $\frac{\partial \mathbf{K}}{\partial F_j} = 0$. Therefore we can solve for each column of the Jacobian with the equation $\mathbf{K} \left\{\frac{\partial \mathbf{u}}{\partial F_j}\right\} = \mathbf{e}_j$. In practice, $\mathbf{d}\left(\mathbf{v}_l + \mathbf{u}_l(\mathbf{x}), \mathbf{S}_f\right)$ can be looked up in the precomputed vector distance map of the fixed organ, $\mathbf{S}_f$, and the derivatives $\partial \mathbf{d} / \partial u_j$ can be approximated with a centered finite difference operator applied on the map. Fig. 4b shows one of the distance maps used in our experiments. Notice that the physical model can be different, as long as the derivatives $\partial u_i / \partial x_j$ can be computed.

In our experiments, however, we observed that the magnitudes of gradients with respect to the material properties, $\|\partial\Phi/\partial\mathbf{E}\|$, are about 1000 times smaller than that with respect to the forces, $\|\partial\Phi/\partial\mathbf{F}\|$, which caused the material properties to converge very slowly. To obtain a faster convergence of $\mathbf{E}$, we embed the optimization of the forces into the objective function evaluation at each $\mathbf{E}$ value. That is, every time $\Phi(\mathbf{E})$ is evaluated, a full optimization of $\mathbf{F}$ is performed with the fixed value of $\mathbf{E}$.

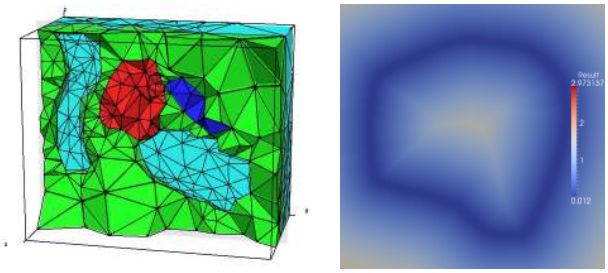

(a) (b)

Figure 4: Input to our algorithm: (a) a sliced view of the tetrahedral model of the moving image (light-blue triangles represent surfaces, not FEM regions; bladder and rectum are hollow); (b) a slice of the distance map of the prostate surface in the reference image.

D. Numerical Optimization

We use a line search scheme for optimization: in each iteration k, we find a descent direction $\mathbf{p}_k$, find an optimal step size α in that direction with a line search algorithm, and then update the parameters with $\mathbf{x}_{k+1} = \mathbf{x}_k + \alpha \mathbf{p}_k$. The descent direction can be computed by using Newton's method to solve the equation $\nabla\Phi = 0$: $\mathbf{p}_k = -\mathbf{B}_k^{-1} \nabla\Phi(\mathbf{x}_k)$, where $\mathbf{B}$ is the Hessian matrix, $\left[\frac{\partial^2 \Phi}{\partial x_i \partial x_j}\right]$. A modified Newton's method has been used in elasticity reconstruction [15], but the Hessian matrices can only be approximated and are usually ill-conditioned. Alternatively, we can use a Quasi-Newton method such as the BFGS formula to avoid computing the Hessian [36].

Quasi-Newton methods can reduce the computation yet still retain a super-linear convergence rate. A line search enforcing the curvature condition ($\mathbf{s}_k^T \mathbf{y}_k > 0$) needs to be performed to keep the approximate Hessian positive definite. In our case, the number of parameters can be in the thousands, and therefore we adopt a limited-memory quasi-Newton method known as the L-BFGS method [36].

E. Initial Guess of Parameters

A good initial guess can prevent the optimizer from getting stuck in a local minimum. Our initial guess for the forces is based on the distance field of the target surface: each node requiring a boundary condition is moved according to the distance field to compute a Dirichlet boundary condition. A forward simulation is performed using the set of boundary conditions and the initial guess of elasticities, and the output deformation is used, via (1), to compute the corresponding forces, which become the initial guess for the forces.

In the case of medical image registration, the initial guess of the elasticity is chosen based on knowledge of the simulated organs. Our example images involve two materials: the prostate and the surrounding tissue. There have been *ex vivo* experiments on the prostate using different elasticity models.

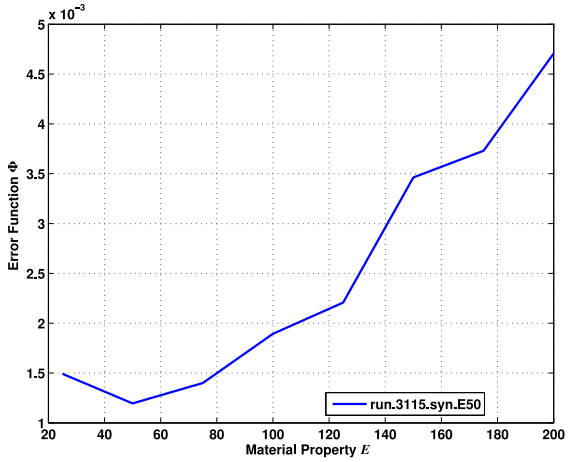

Figure 5: Plot of Φ and $\mathbf{E}$ (in kPa) with several sample values for finding an initial guess of elasticity value in a synthetic multi-organ scene. The plot suggests that the best initial guess is 50 kPa.

Krouskop et al. [37] reported an elastic modulus of 40-80 kPa for normal prostate tissue, 28-52 kPa for BPH tissue, and 80-260 kPa for cancerous tissue when receiving 4% compression. They also reported 10-30 kPa for breast fat tissue. Based on these numbers for fat tissue, we chose an elasticity value of 10 kPa for the tissue surrounding the prostate. This value is fixed, in our calculations, since only the ratio of the elasticity values matters.

The initial guess of elasticity for the prostate is chosen by a parameter search: we perform force optimizations with several elasticity values between 30 kPa and 200 kPa and choose the elasticity with the lowest objective function value after the force optimization. An example result of the parameter search is shown in Fig. 5, where the target surfaces are generated by artificially deforming a set of organ boundaries, so that we know the true elasticity value. The plot shows that the parameter search successfully located the global minimum in the synthetic case with multiple organs. In our experiments using synthetic and real organ boundaries of the male pelvis area, we have observed similar curves with a single minimum. If more than one local minimum is observed, an optimization can be performed using each of these values as the initial guess. To reduce the computation time, we use a lower-resolution mesh for the parameter search, and the resulting optimal forces are used as the initial guess when using a higher-resolution mesh for elasticity optimization.

III. Experiments

We used the male pelvis area as the test scene. To build the reference surfaces, we obtained segmentations of a 3D CT image of the male pelvis area, including the surfaces of the bladder, prostate, rectum, and bones. A tetrahedral finite element mesh is constructed from a set of reference surfaces, as shown in Fig. 4a. The corresponding target surfaces are used to compute the distance map, as shown in Fig. 4b. In the tetrahedral mesh, the bladder and the rectum are made hollow to reflect the actual structure, and the bones are fixed during the simulations. Since the prostate is the main organ of interest, we apply forces only on the boundaries of the bladder and the rectum to reduce the uncertainty on the prostate, which will be moved by surrounding tissues. The setting also reflects the fact that the bladder and the rectum are the organs that have larger deformations due to different amount of fluid and gas, and the prostate is usually deformed by their movement.

During the iterative optimization, the objective function is evaluated over the surfaces of the bladder, rectum, and prostate. The Poisson's ratios are fixed (0.40 for the prostate and 0.35 for surrounding tissues, chosen based on literature in image registration [29], [38], [31]), and we optimize for the elasticity values because of its importance in noninvasive cancer detection. Since only the relative values of material properties can be recovered, we fix the Young's modulus of the surrounding tissues (the region outside all organs and bones) to 10 kPa and optimize that of the prostate.

We tested our algorithm on two types of surface data. First, we tested the accuracy of the optimization scheme using synthetic target surfaces generated by forward simulations, so that we know the true elasticity values. We then applied the technique to prostate cancer stage assessment based on multiple segmented target images of the same patient to show applicability to real data. Since the distances between reference and target surfaces are minimized, we also compare the visual result (the warped image) with that of an image-based image registration method.

The reference and target organ surfaces are obtained from real 3D CT images of the male pelvis area using the software MxAnatomy (Morphormics, Durham, NC), and the bones are segmented using ITK-SNAP [39]. Given the moving surfaces in the form of triangle meshes, the tetrahedral model for the entire domain is built with the software TetGen [40], and the library ITK [41] is used to compute the vector distance maps of the target surface. The FEM simulator uses the linear algebra library PETSc [42].

Mesh generation: The image segmentation was done with an early semi-automatic version of software MxAnatomy. For the prostate, the user typically needed to specify 15-20 initial boundary points on five image slices, and it usually took 20 minutes to segment the three main organs (prostate, bladder, and rectum) in a CT image. The semi-automatic segmentation of bones (ITK-SNAP) requires some initial pixels (specified with a few spheres) that are roughly in line with the bones, and the algorithm iteratively grows or shrinks from these initial pixels until an optimal binary image of the bone is achieved. It usually takes 15 minutes for the segmentation of bones. Once the surface meshes are generated, the tetrahedralization takes a few seconds using the software TetGen.

A. Synthetic Scene with Multiple Organs

To test how well our algorithm recovers elasticity values, we use synthetic target surfaces generated with known elasticity and boundary conditions. The target surfaces are generated by a forward simulation with Dirichlet boundary conditions acquired from a real pair of segmented images applied to the bladder and rectum surfaces. The moving surfaces and

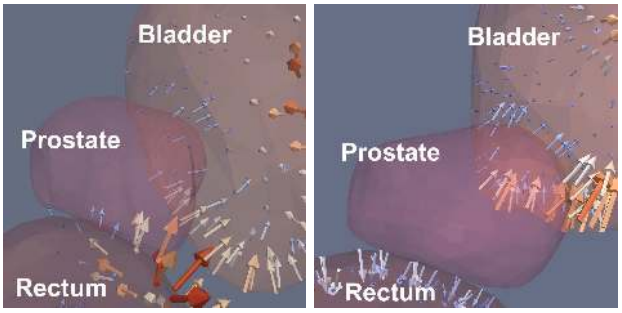

Figure 6: The moving surfaces and ground-truth boundary conditions in the two synthetic multi-organ scenes: the arrows shows Dirichlet boundary conditions applied to surfaces of bladder and rectum; the scaling of arrows are according to the magnitude of displacements.

boundary conditions in the two synthetic scenes are shown in Fig. 6, where the boundary conditions are shown with scaled 3D arrows. The elasticity value of the prostate is controlled, and we can therefore compare the value recovered by our method to the ground truth. We tested our algorithm with three elasticity values, and the results are shown in Table I. The optimization process is terminated when $\|\partial\Phi/\partial\mathbf{E}\| < 10^{-7}\,\|\mathbf{E}\|$ and $\|\partial\Phi/\partial\mathbf{F}\| < 10^{-4}\,\|\mathbf{F}\|$, or when the optimizer cannot find a direction in the parameter space that reduces the value of the objective function. The relative error is less than 12% in the cases where the elasticity values do not exceed 150 kPa, which corresponds to an elasticity ratio of 15 between the prostate and the surrounding tissue. Notice that according to the literature [37], the ratio is already beyond the range for normal tissues and is within the range for cancerous tissues. Therefore we expect to see worse accuracy in the case of stiffer cancerous tissues.

Effect of inaccurate Poisson's ratios: In order to show the effect of selecting different Poisson's ratios, we repeat the experiments using synthetic target surfaces generated with five different Poisson's ratios for the prostate (0.3, 0.35, 0.4, 0.45, and 0.49), while the assumed value is fixed to 0.4 during the optimization process. (Most previous work on image registration or elastography assumes values between 0.3 and 0.49). As shown in Fig. 7, the relative errors in recovered elasticity increase with larger deviation of the Poisson's ratio, and the effect is especially prominent in the cases with lower elasticity values (soft) and low Poisson's Ratios (compressible). We observe errors of 45–60% with an elasticity of 50 kPa and a Poisson's ratio of 0.3. The errors are generally below 13.3% in cases with Poisson's ratios of 0.40–0.45 and can be as high as 20% for a ratio of 0.49 (nearly incompressible). These results show that our method is robust to inaccurate Poisson's ratios in most cases.

B. Noninvasive Assessment of Prostate Cancer Stage

To show the effectiveness of our method applied to prostate cancer assessment, we repeated the experiments on the multi-organ settings, but with both the deformed and target surfaces taken from segmented 3D CT images of the male pelvis area. We consider 10 patient data sets (a total of 112 target images)

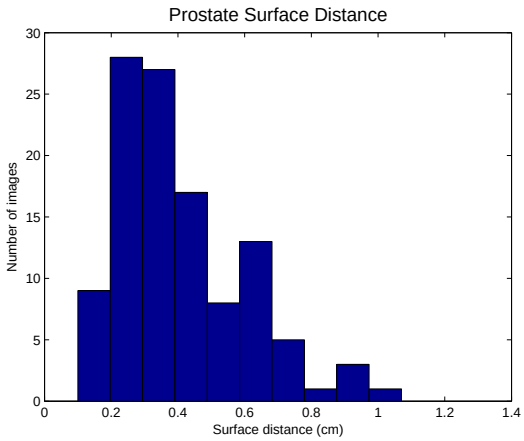

Figure 8: Histogram of distances between the pairs of corresponding reference and target prostate meshes used in our experiments on segmented CT images.

taken throughout courses of radiotherapy for prostate cancer. Each patient data set consists of a set of reference surfaces (bladder, prostate, rectum, and bones), which is from the CT image (reference image) taken before the radiotherapy, and multiple sets of target surfaces, each of them representing the internal structures in one daily CT image during the therapy. The reference image is taken about a week before the first treatment, and treatment (target) images are typically taken twice a week. For each patient data set, we repeated the process of deforming the reference surfaces toward a set of target surfaces with our method, so that one elasticity value of the prostate is recovered for each daily image. Fig. 8 shows the histogram of surface-surface distance between pairs of reference and target prostate surfaces used in the experiments. The surface-surface distance is defined as the maximum of node-surface distance,

$$\max_{\mathbf{v}_l \in \mathbf{S}_m} \mathbf{d}(\mathbf{v}_l, \mathbf{S}_f), \tag{5}$$

where $\mathbf{S}_m$ is the reference (moving) prostate surface, and $\mathbf{S}_f$ is the target surface. The average surface distance for the prostate among the 112 pairs of images is 0.41 cm, which is less than 10% of the diameter of a typical prostate (around 4–5 cm).

The convergence graphs (plots of Φ and $\|\nabla\Phi\|$ versus iteration number) and for boundary forces and for the material property from a typical image pair are shown in Fig. 9 (convergence graphs for other experiments are similar). Note that the optimization of forces was done in batches (in each evaluation of $\Phi(\mathbf{E})$), and the convergence graph for force optimization is the result of concatenating the steps for optimizing $\mathbf{F}$. With our current code, each iteration for the force optimizer takes about 19 seconds for a mesh with 34,705 tetrahedral elements and 6,119 nodes on a Xeon X3440 CPU, and the total number of iterations is around 1,700 (the total time is about nine hours), which means that our current implementation is only suitable for off-line processes. Note that we have not utilized any parallelism in the FEM computation. In the future, we plan to explore faster implementations of the FEM, such as those utilizing a many-core processor and reduced-dimension

Table I: Error in recovered modulus of elasticity in two synthetic multi-organ scenes; note that the error becomes much larger for elasticity values greater than 150 kPa.

True Elasticity (kPa)		50	100	150	200	250	300	350
Scene 1	Recovered Value	49	101.18	158.79	141.57	136.65	204.45	176
	Relative Error	-2%	+1.2%	+5.9%	-29.2%	-45.3%	-31.9%	-49.7%
Scene 2	Recovered Value	51.33	102.90	167.5	225.0	222.91	275.0	277.97
	Relative Error	+2.7%	+2.9%	+11.7%	+12.5%	-10.8%	-8.3%	-20.6%

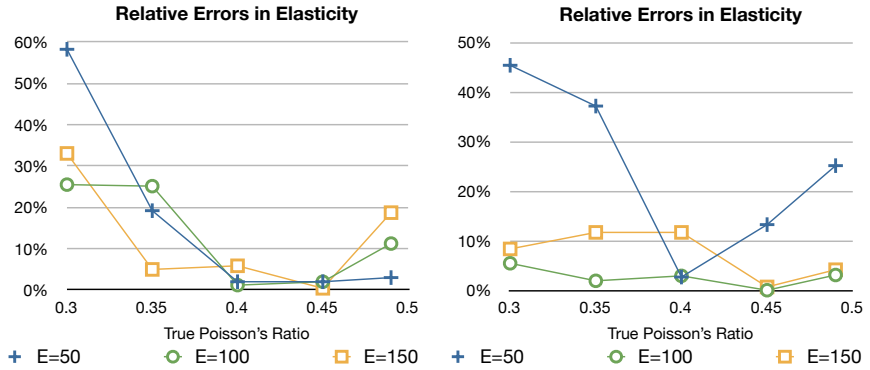

Figure 7: Plots of relative errors in recovered elasticity vs. different Poisson's ratios for the prostate (0.3, 0.35, 0.4, 0.45, and 0.49) used for generating the synthetic surface data; each plot shows the result from one test scene, and each curve represents a true elasticity value (50, 100, and 150 kPa) used in the synthetic case. During the optimization process, the assumed Poisson's ratio is always fixed to 0.4.

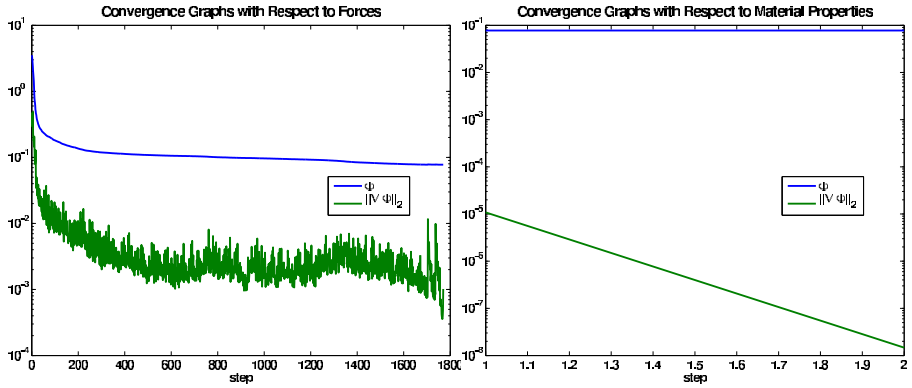

Figure 9: Convergence graphs (plot of Φ and $\|\nabla\Phi\|$ versus iteration number) for a pair of CT image data: (left) convergence of the external forces; (right) convergence of the elasticity.

models.

Each of the 10 patient data sets tested include 6 to 17 sets of target surfaces (daily images), namely 112 target images in total, and the recovered elasticity values of the prostate for each patient are shown in Table II. Notice that the recovered values from all image pairs are within the range suggested in the literature [37], and the result shows consistency within each patient.

The aim of this study is to assess the relation between the recovered elasticity value and the cancer stage of each patient, under the assumption that prostates with more advanced tumors have higher stiffness. A common cancer staging system is the TNM (Tumor, lymph Nodes, Metastasis) system, where the clinical T-stage describes the size and extent of the primary tumor [43]. The definitions of T-stages are shown in Table III. We focus on the T-stage because of its relevance

Table II: Average and standard deviation of elasticity values for the prostate recovered from the patient data sets; the last column is the clinical cancer staging for the tumor for each patient.

	Number of Targets	Average Young's Modulus (kPa)	Std. Deviation	Clinical T-Stage
Patient 1	8	48.60	2.41	T1
Patient 2	6	53.99	10.28	T3
Patient 3	7	71.97	4.35	T3
Patient 4	6	60.81	1.25	T2
Patient 5	16	38.06	13.91	T1
Patient 6	16	45.42	10.26	T1
Patient 7	17	40.67	16.34	T2
Patient 8	15	52.40	7.72	T2
Patient 9	9	51.47	7.50	T1
Patient 10	12	56.19	7.95	T2

Table III: Definition of clinical T-stages for prostate cancer

Stage	Definition
TX	Primary tumor cannot be assessed
T0	No evidence of primary tumor
T1	Clinically inapparent tumor neither palpable nor visible by imaging
T2	Tumor confined within prostate
T3	Tumor extends through the prostate capsule
T4	Tumor is fixed or invades structures other than seminal vesicles

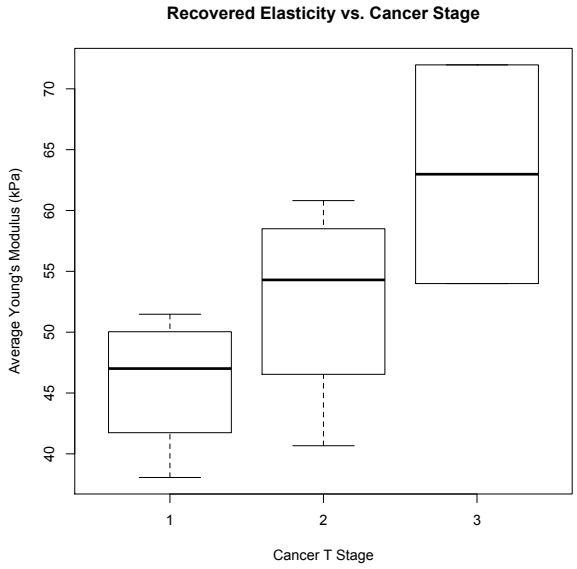

Figure 10: Box plot of average recovered elasticity value and cancer T stage for each patient data set shown in Table II.

to the stiffness of the prostate. The clinical T-stages for the patients are shown in the last column of Table II. In order to analyze the data statistically, we treat the average recovered elasticities and tumor stages as two random variables and use numbers 1, 2, and 3 to represent T-stages T1, T2, and T3, respectively (T0 and T4 are not present in our data sets), and we test if the recovered elasticity values and the T-stages are positively correlated. The resulting Pearson (linear) correlation coefficient is 0.662, and the p-value for the two-sided correlation test is 0.037, which indicates a significant positive correlation between the recovered elasticity values and the T-stages, based on a p-value threshold of 0.05. Since the tumor stage values are discrete and might be nonlinear with respect to the elasticity, a rank correlation coefficient, such as the Spearman's rank correlation ρ, may be more suited for the test. From the samples we have Spearman's $\rho = 0.701$ and an estimated p-value of 0.024, which shows again a significant positive correlation. The box plot of the elasticity values and cancer stages is shown in Fig. 10.

C. Study: Inhomogeneous Materials

We assume a constant material property within an organ due to the limitation of the image modality, where the intensity is almost constant within the prostate, so that it is impossible to segment the tumor. The elasticity values recovered by our method are therefore "average" values in some sense, and a higher recovered elasticity indicates either a stiffer tumor or a larger tumor. Since the clinical T-stage for prostate cancer depends on the extent of the tumor, we conducted a study to show the correlation between the tumor size and the recovered elasticity value. Based on the settings in the synthetic multi-organ experiments in Section III-A, we embedded an additional tumor inside the prostate for generating synthetic target surfaces, as shown in Fig. 11. The elasticity values for the tumor and the normal prostate tissues are set to 100 and 50 kPa, respectively. Notice that in the elasticity recovery process, we do not know the extent of the tumor due to the imaging limitation, and we only recover one value for the prostate. Table IV shows the recovered elasticity values with different tumor sizes relative to the entire prostate. The results show increasing elasticity values with increasing tumor sizes in both scenes. Even though we assume homogeneous materials, the recovered values can still be used as an indicator of the extent of the tumor and are therefore correlated to cancer stages.

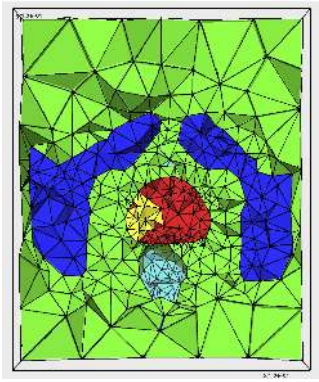

Figure 11: A sliced view of the tetrahedral mesh with a tumor (yellow) embedded in the prostate (red); the mesh is used to generate the synthetic target surface, while the prostate is still considered homogeneous in the optimization process.

Table IV: The recovered elasticity values for the prostate as a homogeneous material, when the organ contains a synthetic tumor of different sizes and a normal tissue; elasticity values are set to 100 kPa for the tumor and 50 kPa for normal prostate tissue.

	tumor size / prostate size (%)			
	10%	25%	50%	75%
Scene 1	51.24	54.98	62.15	63.44
Scene 2	53.55	56.90	69.62	70

D. Application: Registration of Segmented CT Images

Since the distance between the fixed and moving surfaces is minimized during the optimization process, we also have an image registration as a result of optimizing for forces and elasticities. In our experiments, the final average value of the objective function is 0.09, corresponding to an RMS error of 0.01 cm, and a maximum of 0.22 cm, which are within the image resolution, $0.1 \times 0.1 \times 0.3$ cm. The deformed images of a typical image pair before and after registration are shown in Fig. 13, with the segmentations of the reference image (red)

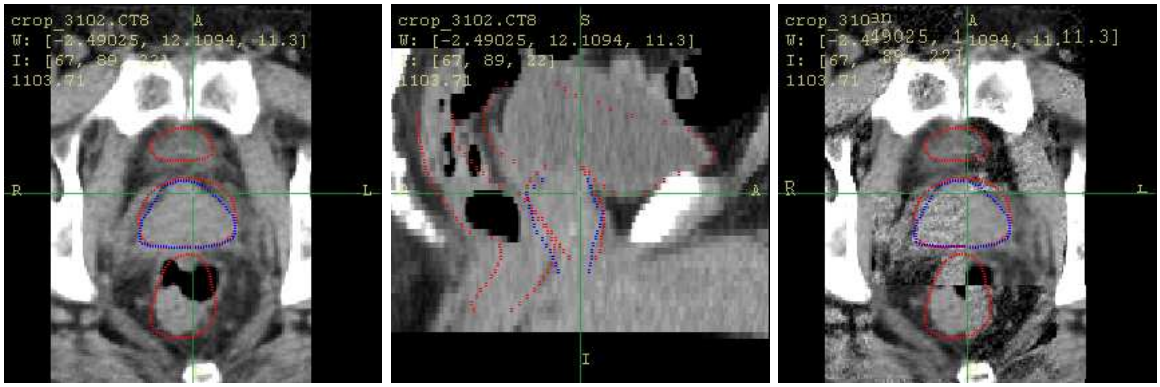

(a)

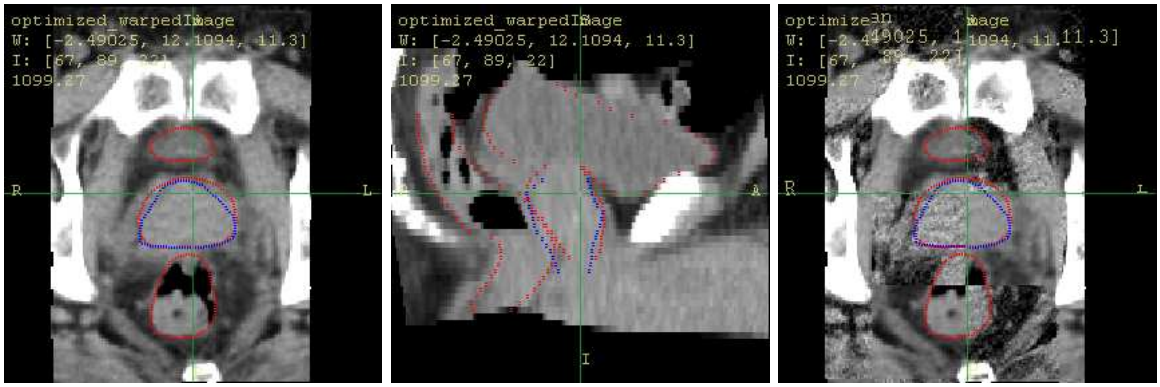

(b)

Figure 13: Registration results for a pair of test images: (a) axial and sagittal views of the moving image, and a 4x4 checkerboard comparison with the planning image, before registration; (b) the two views of the registered image, along with a checkerboard comparison with the planning image; superimposed by segmentations of the reference image, shown in red, and the segmentation of the prostate in the daily image, shown in blue; notice that the image deforms towards the red contours.

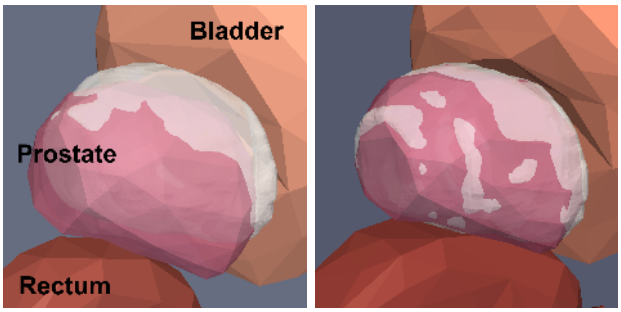

Figure 12: Close-up view of the surfaces before (left) and after (right) deformation; the transparent white surface shown is the target surface of the prostate. Notice how the prostate surface move towards the white surface. Bladder and rectum surfaces are those with external forces applied.

and the prostate in the moving image (blue) superimposed on the image. Notice how the prostate in the images moves from the blue contour to the red contour. Fig. 12 shows a 3D close-up view of the deforming surfaces from another image pair, where the surfaces of the bladder and the rectum are those with external forces applied, and the target surface of the prostate is shown in white.

We also compared our registration results with a popular image-based approach, the Demons method [44], by looking at some landmarks inside the prostate. In most cases, the image intensity is almost constant inside an organ, but five of the patient data sets (a total of 32 image pairs) we experimented on have three "seeds" implanted in the prostate for location tracking during each treatment fraction, resulting in bright spots that can be observed in the CT image. The distance between the target and the deformed landmark positions from the two methods are shown in Table V, and the two-tail t-tests for paired samples (distances) show that our method produces statistically significantly better results in three out of five patient data sets (with a p-value threshold of 0.05). For regions with nearly uniform intensity, the deformation computed by the Demons method is entirely governed by the registration regularization terms, which do not need to be physically meaningful for the image-based method. Our method enforces physically-based constraints and results in errors within the diameter of the spot. Notice that for the Demons method, we replaced the voxel values inside the prostate with the average intensity within the organ, since the intensity and gradient information from the landmarks could also be utilized in the image-based registration, giving it an additional advantage, while our method is based purely on the physics-based simulation and does not take advantage of the landmarks.

Table V: Average error in landmark positions (distance in cm) inside the prostate, computed with the Demons method and our method; t-tests show that our method performs statistically significantly better in three of the five data sets.

	# Target Images	Demons		Our Method		Paired t-test p-value
		Avg. (cm)	Std. dev.	Avg. (cm)	Std. dev.	
Patient 1	8	0.27	0.17	0.26	0.18	0.07
Patient 2	6	0.21	0.11	0.16	0.11	0.03
Patient 3	7	0.18	0.06	0.10	0.04	1.5e-4
Patient 4	6	0.17	0.07	0.13	0.03	0.02
Patient 5	5	0.21	0.15	0.20	0.08	0.86

Table VI: Error in recovered nonlinear modulus of elasticity in two synthetic multi-organ scenes.

True Elasticity (kPa)		50	100	150	200
Scene 1	Recovered Value	50.18	105.64	159	174
	Relative Error	+0.35%	+5.6%	+6%	-13%
Scene 2	Recovered Value	45	105	141.5	197
	Relative Error	-10%	+5%	-5.67%	-1.5%

E. Extension: Nonlinear FEM

To demonstrate that our optimization framework can also be applicable to nonlinear models, we incorporated a geometrically nonlinear FEM and the neo-Hookean model with the elasticity optimization scheme. The linearized equilibrium formulation of the nonlinear FEM is

$$\mathbf{K}(\mathbf{u}^n) \cdot \Delta\mathbf{u} = \mathbf{f}^{\text{ext}} - \mathbf{f}^{\text{int}}, \tag{6}$$

where $\mathbf{f}^{\text{ext}}$ and $\mathbf{f}^{\text{int}}$ are the external and internal force vectors, $\mathbf{K}(\mathbf{u}^n)$ is the stiffness matrix that depends on the current displacement vector $\mathbf{u}^n$, and $\Delta\mathbf{u}$ is used to update the vector $\mathbf{u}^n$ in a Newton iteration ($\mathbf{u}^{n+1} = \mathbf{u}^n + \Delta\mathbf{u}$). The Jacobian matrix $\mathbf{J}_u = \left[\frac{\partial u_i}{\partial E_j}\right]$ (derivative of displacements $\mathbf{u}$ with respect to the elasticity parameter E_j) for the elasticity optimizer is approximated using the finite difference method due to the complexity of differentiating the internal forces with respect to the elasticity. Notice that we have not implemented force optimization for the nonlinear model, and boundary conditions given by a surface matching is always used in the simulation.

1) Synthetic scene with multiple organs: We used the same multi-organ scenes in Section III-A and deformed them using the nonlinear FEM to generate the synthetic target surfaces. That is, the nonlinear FEM is used in both generating synthetic cases and in the optimization scheme. The resulting recovered elasticity values are shown in Table VI. The errors are within 13% for the range we tested (50-200 kPa).

Effect of inaccurate elasticity values for surrounding tissues: The elasticity value for tissue surrounding the prostate is fixed to 10 kPa in our experiments. While only the ratio between two elasticity values can be recovered with a linear model without knowing true force values (as discussed in Section II-A), the surrounding tissue elasticity could have a different effect on nonlinear models. However, with the small amount of displacement we have observed, we expect the surrounding tissue elasticity to have a similar effect as in the linear model. For example, if the true elasticity values for the prostate and surrounding tissue are 100 kPa and 20 kPa, respectively, we expect to recover the value 50 kPa for the prostate since the surrounding tissue elasticity is fixed to 10 kPa in the optimization. Table VII shows the results using the nonlinear FEM where the true elasticity is twice the value used in the optimization process. The recovered elasticities for the prostate are very close to what we expect, with relative errors below 13%.

Table VII: Error in recovered nonlinear modulus of elasticity in two synthetic multi-organ scenes where the elasticity of surrounding tissue is doubled (20 kPa) when generating the synthetic data. The surrounding tissue elasticity is still set to 10 kPa in the optimization process, and we expect to see recovered values for the prostate to be half of the true values.

Elasticity for Surroundings		20 kPa			
Elasticity for Prostate (kPa)		50	100	150	200
Expected Value for Prostate		25	50	75	100
Scene 1	Recovered Value	28.05	50.17	72.98	106.17
	Relative Error	+12.2%	+0.34%	-2.7%	+6.17%
Scene 2	Recovered Value	25	45	76.52	108.16
	Relative Error	0%	-10%	+2.02%	+8.16%

2) Assessment of prostate cancer stage: We repeated the experiments in Section III-B using the nonlinear FEM. The recovered elasticity values for the 10 patient data sets are shown in Table VIII, and the box plot of average recovered elasticity and clinical T-stage is shown in Fig. 14. The Pearson (linear) correlation coefficient for recovered elasticity values and T-stages is 0.704 with a p-value of 0.023, and the Spearman's rank correlation ρ is 0.636 with a p-value of 0.048, which again shows a significant positive correlation between the stiffness value and the cancer stage for this group of patients. However, the recovered values are less consistent than those from the linear FEM implementation. We conjecture that the implementation using nonlinear FEM is more sensitive to the material properties and boundary conditions, and therefore the recovered values vary more than those using the linear FEM.

IV. Conclusion and Future Work

We have presented a novel physically-based method for simultaneously estimating the 3D deformation of soft bodies and determining the unknown material properties and boundary conditions. Previous elastography methods are limited by imaging modalities and force measurement schemes, and we overcome these limitations by utilizing the surface information extracted from 3D images. Although the resolution of the resulting elastogram is limited to the object boundaries, we showed that the recovered value reflects the distribution of materials within the object, and the recovered elasticity values

Table VIII: Average and standard deviation of elasticity values for the prostate recovered from the patient data sets using nonlinear FEM; the last column is the clinical cancer staging for the tumor for each patient.

	Average Young's Modulus (kPa)	Std. Deviation	Clinical T-Stage
Patient 1	47.29	3.25	T1
Patient 2	69.28	8.09	T3
Patient 3	78.91	4.81	T3
Patient 4	63.62	2.92	T2
Patient 5	47.45	16.62	T1
Patient 6	59.85	18.37	T1
Patient 7	62.73	18.34	T2
Patient 8	60.23	11.93	T2
Patient 9	69.74	11.46	T1
Patient 10	69.25	17.64	T2

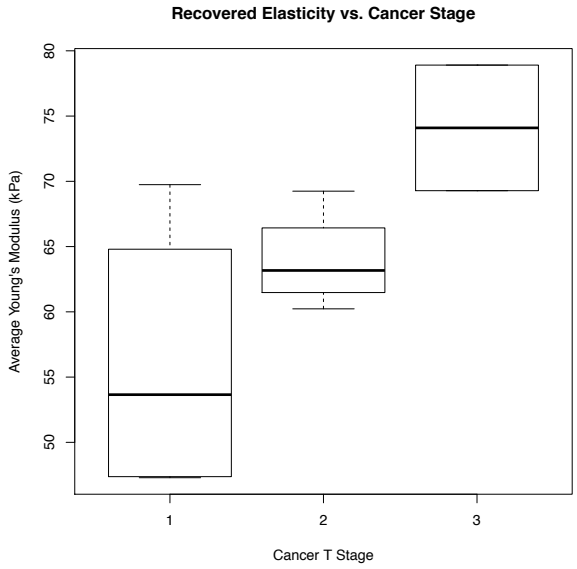

Figure 14: Box plot of average recovered nonlinear elasticity value and cancer T stage for each patient data set shown in Table VIII.

have a significant positive correlation with clinical prostate cancer staging in small-scale experiments. Therefore, our method has the potential to become a means of noninvasive cancer detection.

As a non-rigid image registration method, ours automatically determines the patient-specific material properties during the registration. The resulting deformation field is enforced to be physically plausible, since it is computed by the 3D FEM simulator with appropriate contact constraints among organs. The observed error on the boundary is within the resolution of the segmented images, and the error on the internal bright spots as landmarks in the prostate is comparable to the diameter of the spots.

The optimization framework for joint estimation of both 3D deformation and material parameters is generalizable. It is not limited to elasticity reconstruction and could be used for more sophisticated physiological models than the basic linear and nonlinear elasticity models we chose for simplicity in our current implementation. As an image registration technique, our method is reliable in terms of the registration error; as a parameter estimation method, our system can save an enormous amount of efforts adjusting the simulation parameters manually by automatically extracting patient-specific tissue properties. Furthermore, since only the 3D surfaces are used in our algorithm, applications other than medical image analysis could also adopt the method.

Our current implementation assumes that the Poisson's ratio can be treated as known, which is also the case in most elastography studies, since the Young's modulus has more clinical significance in cancer detection. However, it has been reported that the Poisson's ratio plays a more important role than the elasticity in modeling deformation of breasts [38], where the optimal Poisson's ratio also depends on the boundary conditions — lower values could improve the results when volume changes need to be modeled. Therefore, a study of how different Poisson's ratios affect elastography results could be a topic for future investigation.

In the near future, we plan to accelerate performance of the iterative scheme by many-core computing and model reduction. The resulting implementation can then be applied to more complicated physical and geometric models, such as situations with complex material property distributions, surface sliding, and large deformations. We would also like to explore the possibility of clinical trials of our method to noninvasive cancer staging based on the stiffness value. Virtual surgery and material engineering are some example application domains that would benefit from an automatic estimation of material properties and they can also directly benefit from this framework, worthy of further exploration.

ACKNOWLEDGMENT

We thank Ed Chaney and Ron Alterovitz for helpful discussions. We also thank Zijie Xu and Dr. Ron Chen in the UNC Department of Radiation Oncology for providing prostate patient data. This work was partially supported by grants NIH R44 CA119571, ARO W911NF0610355, NSF CMMI-1000579, NSF EECS-1148870, NSF EECS-0925875, and Carolina Development Foundation.

REFERENCES

[1] M. Kauer, V. Vuskovic, J. Dual, G. Szekely, and M. Bajka, "Inverse finite element characterization of soft tissues," *Medical Image Analysis*, vol. 6, pp. 275–287, Sept. 2002.

[2] C. Syllebranque and S. Boivin, "Estimation of mechanical parameters of deformable solids from videos," *The Visual Computer*, vol. 24, no. 11, pp. 963–972, 2008.

[3] J. Ophir, S. Alam, B. Garra, F. Kallel, E. Konofagou, T. Krouskop, and T. Varghese, "Elastography: ultrasonic estimation and imaging of the elastic properties of tissues," *Proceedings of the Institution of Mechanical Engineers, Part H: Journal of Engineering in Medicine*, vol. 213, pp. 203–233, Jan. 1999.

[4] A. Manduca, T. E. Oliphant, M. A. Dresner, J. L. Mahowald, S. A. Kruse, E. Amromin, J. P. Felmlee, J. F. Greenleaf, and R. L. Ehman, "Magnetic resonance elastography: Non-invasive mapping of tissue elasticity," *Medical Image Analysis*, vol. 5, pp. 237–254, Dec. 2001.

[5] O. C. Zienkiewicz and R. L. Taylor, *The Finite Element Method*. Butterworth-Heinemann, Oxford, 6 ed., Dec. 2005.

[6] A. Skovoroda and S. Emelianov, "Tissue elasticity reconstruction based on ultrasonic displacement and strain images," *IEEE Transactions on Ultrasonics, Ferroelectrics, and Frequency Control*, vol. 42, no. 4, p. 141, 1995.

[7] J. E. Lindop, G. M. Treece, A. H. Gee, and R. W. Prager, "3D elastography using freehand ultrasound," *Ultrasound in Medicine & Biology*, vol. 32, pp. 529–545, Apr. 2006.

[8] H. Rivaz, E. Boctor, P. Foroughi, R. Zellars, G. Fichtinger, and G. Hager, "Ultrasound elastography: A dynamic programming approach," *Medical Imaging, IEEE Transactions on*, vol. 27, no. 10, pp. 1373–1377, 2008.

[9] S. E. Salcudean, D. French, S. Bachmann, R. Zahiri-Azar, X. Wen, and W. J. Morris, "Viscoelasticity modeling of the prostate region using vibro-elastography," in *Medical Image Computing and Computer-Assisted Intervention – MICCAI 2006*, vol. 4190, pp. 389–396, Springer Berlin Heidelberg, 2006.

[10] L. Zhai, T. J. Polascik, W.-C. Foo, S. Rosenzweig, M. L. Palmeri, J. Madden, and K. R. Nightingale, "Acoustic radiation force impulse imaging of human prostates: Initial in vivo demonstration," *Ultrasound in Medicine & Biology*, vol. 38, pp. 50–61, Jan. 2012.

[11] Y. Zhu, T. Hall, and J. Jiang, "A finite-element approach for young's modulus reconstruction," *Medical Imaging, IEEE Transactions on*, vol. 22, no. 7, pp. 890–901, 2003.

[12] M. Becker and M. Teschner, "Robust and efficient estimation of elasticity parameters using the linear finite element method," *Proc. of Simulation and Visualization*, pp. 15–28, 2007.

[13] H. Eskandari, S. E. Salcudean, R. Rohling, and I. Bell, "Real-time solution of the finite element inverse problem of viscoelasticity," *Inverse Problems*, vol. 27, p. 085002, Aug. 2011.

[14] D. S. Schnur and N. Zabaras, "An inverse method for determining elastic material properties and a material interface," *International Journal for Numerical Methods in Engineering*, vol. 33, no. 10, pp. 2039–2057, 1992.

[15] F. Kallel and M. Bertrand, "Tissue elasticity reconstruction using linear perturbation method," *Medical Imaging, IEEE Transactions on*, vol. 15, no. 3, pp. 299–313, 1996.

[16] S. Balocco, O. Camara, and A. F. Frangi, "Towards regional elastography of intracranial aneurysms," in *Medical Image Computing and Computer-Assisted Intervention*, vol. 11, pp. 131–8, 2008. PMID: 18982598.

[17] C. W. Washington and M. I. Miga, "Modality independent elastography (MIE): a new approach to elasticity imaging," *IEEE Trans. on Medical Image*, vol. 23, no. 9, pp. 1117–1128, 2004.

[18] P. Courtis and A. Samani, "Detecting mechanical abnormalities in prostate tissue using FE-Based image registration," in *MICCAI 2007* (N. Ayache, S. Ourselin, and A. Maeder, eds.), vol. 4792 of *Lecture Notes in Computer Science*, pp. 244–251, Springer Berlin / Heidelberg, 2007.

[19] L. Han, J. H. Hipwell, C. Tanner, Z. Taylor, T. Mertzanidou, J. Cardoso, S. Ourselin, and D. J. Hawkes, "Development of patient-specific biomechanical models for predicting large breast deformation," *Physics in Medicine and Biology*, vol. 57, pp. 455–472, Jan. 2012.

[20] P. Risholm, E. Samset, and W. Wells, "Bayesian estimation of deformation and elastic parameters in non-rigid registration," *Biomedical Image Registration*, p. 104–115, 2010.

[21] V. Egorov, S. Ayrapetyan, and A. Sarvazyan, "Prostate mechanical imaging: 3-d image composition and feature calculations," *Medical Imaging, IEEE Transactions on*, vol. 25, pp. 1329 –1340, Oct. 2006.

[22] R. Chopra, A. Arani, Y. Huang, M. Musquera, J. Wachsmuth, M. Bronskill, and D. Plewes, "In vivo MR elastography of the prostate gland using a transurethral actuator," *Magnetic Resonance in Medicine*, vol. 62, no. 3, pp. 665–671, 2009.

[23] M. Sermesant, P. Moireau, O. Camara, J. Sainte-Marie, R. Andriantsimiavona, R. Cimrman, D. L. G. Hill, D. Chapelle, and R. Razavi, "Cardiac function estimation from MRI using a heart model and data assimilation: Advances and difficulties," *Medical Image Analysis*, vol. 10, no. 4, pp. 642–656, 2006.

[24] P. Moireau, D. Chapelle, and P. L. Tallec, "Joint state and parameter estimation for distributed mechanical systems," *Computer Methods in Applied Mechanics and Engineering*, vol. 197, pp. 659–677, Jan. 2008.

[25] J. Maintz and M. A. Viergever, "A survey of medical image registration," *Medical Image Analysis*, vol. 2, pp. 1–36, Mar. 1998.

[26] M. Holden, "A review of geometric transformations for nonrigid body registration," *Medical Imaging, IEEE Transactions on*, vol. 27, no. 1, pp. 111–128, 2008.

[27] M. Ferrant, S. K. Warfield, C. R. G. Guttmann, R. V. Mulkern, F. A. Jolesz, and R. Kikinis, "3D image matching using a finite element based elastic deformation model," in *MICCAI*, pp. 202–209, 1999.

[28] M. Ferrant, S. K. Warfield, A. Nabavi, F. A. Jolesz, and R. Kikinis, "Registration of 3D intraoperative MR images of the brain using a finite element biomechanical model," in *MICCAI*, pp. 19–28, 2000.

[29] A. Bharatha, M. Hirose, N. Hata, S. K. Warfield, M. Ferrant, K. H. Zou, E. Suarez-Santana, J. Ruiz-Alzola, A. D'Amico, R. A. Cormack, R. Kikinis, F. A. Jolesz, and C. M. C. Tempany, "Evaluation of three-dimensional finite element-based deformable registration of pre- and intraoperative prostate imaging," *Medical Physics*, vol. 28, no. 12, p. 2551, 2001.

[30] D. Cash, M. Miga, T. Sinha, R. Galloway, and W. Chapman, "Compensating for intraoperative soft-tissue deformations using incomplete surface data and finite elements," *Medical Imaging, IEEE Transactions on*, vol. 24, pp. 1479 –1491, Nov. 2005.

[31] J. M. Hensel, C. Menard, P. W. M. Chung, M. F. Milosevic, A. Kirilova, J. L. Moseley, M. A. Haider, and K. K. Brock, "Development of multiorgan finite element-based prostate deformation model enabling registration of endorectal coil magnetic resonance imaging for radiotherapy planning," *Int. J. Radiation Oncology Bio. Phys.*, vol. 68, no. 5, pp. 1522–1528, 2007.

[32] A. Wittek, K. Miller, R. Kikinis, and S. K. Warfield, "Patient-specific model of brain deformation: Application to medical image registration," *Journal of Biomechanics*, vol. 40, no. 4, pp. 919–929, 2007.

[33] J. Crouch, S. Pizer, E. Chaney, Y.-C. Hu, G. Mageras, and M. Zaider, "Automated finite-element analysis for deformable registration of prostate images," *Medical Imaging, IEEE Transactions on*, vol. 26, pp. 1379 –1390, Oct. 2007.

[34] R. Alterovitz, K. Goldberg, J. Pouliot, I. Hsu, Y. Kim, S. Noworolski, and J. Kurhanewicz, "Registration of MR prostate images with biomechanical modeling and nonlinear parameter estimation," *Medical Physics*, vol. 33, p. 446, 2006.

[35] M. Foskey, B. Davis, L. Goyal, S. Chang, E. Chaney, N. Strehl, S. Tomei, J. Rosenman, and S. Joshi, "Large deformation three-dimensional image registration in image-guided radiation therapy," *Physics in Medicine and Biology*, vol. 50, pp. 5869–5892, 2005.

[36] J. Nocedal and S. Wright, *Numerical Optimization*. Springer, 1999.

[37] T. A. Krouskop, T. M. Wheeler, F. Kallel, B. S. Garra, and T. Hall, "Elastic moduli of breast and prostate tissues under compression," *Ultrasonic imaging(Print)*, vol. 20, no. 4, pp. 260–274, 1998.

[38] C. Tanner, J. A. Schnabel, D. L. G. Hill, D. J. Hawkes, M. O. Leach, and D. R. Hose, "Factors influencing the accuracy of biomechanical breast models," *Medical Physics*, vol. 33, no. 6, p. 1758, 2006.

[39] P. A. Yushkevich, J. Piven, H. C. Hazlett, R. G. Smith, S. Ho, J. C. Gee, and G. Gerig, "User-guided 3D active contour segmentation of anatomical structures: Significantly improved efficiency and reliability," *NeuroImage*, vol. 31, pp. 1116–1128, July 2006.

[40] H. Si, "TetGen: a quality tetrahedral mesh generator and three-dimensional delaunay triangulator," Dec. 2009.

[41] T. S. Yoo, M. J. Ackerman, W. E. Lorensen, W. Schroeder, V. Chalana, S. Aylward, D. Metaxas, and R. Whitaker, "Engineering and algorithm design for an image processing API: a technical report on ITK - the insight toolkit," 2002.

[42] S. Balay, W. D. Gropp, L. C. McInnes, and B. F. Smith, "Efficient management of parallelism in object-oriented numerical software libraries," *Modern Software Tools in Scientific Computing*, pp. 163—202, 1997.

[43] L. H. Sobin, *TNM Classification of Malignant Tumours*. John Wiley and Sons, Dec. 2009.

[44] J.-P. Thirion, "Image matching as a diffusion process: an analogy with maxwell's demons," *Medical Image Analysis*, vol. 2, no. 3, pp. 243–260, 1998.